

Article

Numerical Analysis and Optimization of Flow Rate for Vanadium Flow Battery Incorporating Temperature Effect

Lukang Han ^{1,†}, Hui Chen ^{1,†}, Xiangdong Cheng ¹, Qiang He ¹, Fuyu Chen ^{1,2,*} and Qinfang Zhang ^{1,*} 

¹ School of Materials Science and Engineering, Yancheng Institute of Technology, Yancheng 224051, China

² Jiangsu Provincial Key Laboratory of Eco-Environmental Materials, Yancheng Institute of Technology, Yancheng 224051, China

* Correspondence: hchen@ycit.edu.cn (F.C.); qfangzhang@gmail.com (Q.Z.); Tel.: +86-0515-88298643 (F.C.); Fax: +86-0515-88298249 (F.C.)

† These authors contributed equally to this work.

Abstract: The vanadium flow batteries that employ the vanadium element as active couples for both half-cells, thus avoiding cross-contamination, are promising large-scale energy storage devices. In this work, the flow rate is optimized by incorporating the temperature effects, attempting to realize a more accurate flow control and subsequently enhance the performance of vanadium flow batteries. This work starts with the development of a comprehensive dynamic model on the basis of mass conservation, followed by a modeling validation and a thorough investigation of the temperature effects on electrolyte viscosity and internal resistance. After that, the flow rate is optimized to incorporate such effects. It is found that the flow rate strategy needs to be regulated with the variation of temperature due to the variations of electrolyte viscosity and internal resistance. Moreover, a relatively low flow rate is preferable for low-temperature applications, while for the high-temperature use, a relatively high flow rate is encouraged. Such in-depth investigation can not only provide a cost-effective method to optimize the flow rate and predict the behaviors of vanadium flow batteries, but can also be of great benefit to the management, application, and promotion of vanadium flow batteries.



Citation: Han, L.; Chen, H.; Cheng, X.; He, Q.; Chen, F.; Zhang, Q. Numerical Analysis and Optimization of Flow Rate for Vanadium Flow Battery Incorporating Temperature Effect. *Batteries* **2023**, *9*, 312. <https://doi.org/10.3390/batteries9060312>

Academic Editors: Qing Wang and Leon L. Shaw

Received: 31 March 2023

Revised: 30 May 2023

Accepted: 2 June 2023

Published: 5 June 2023



Copyright: © 2023 by the authors. Licensee MDPI, Basel, Switzerland. This article is an open access article distributed under the terms and conditions of the Creative Commons Attribution (CC BY) license (<https://creativecommons.org/licenses/by/4.0/>).

1. Introduction

Over the years, the problems of energy crisis and environmental pollution have presented concerns due to the extensive consumption of fossil fuels. On the other hand, renewable energy resources, for instance, solar and wind, are restricted in widespread applications on the grid as a result of their intermittent and unstable features [1]. Electrical energy storage (EES), which allows for storing and releasing electricity as needed, is receiving on-going attention to solve such problems [2]. In EES, redox flow batteries (RFBs), which can offer multiple services including peak shaving, power balancing, emergency backup, uninterruptible power supplies, and energy buffers for electric vehicle recharging stations [3,4], are regarded as ideal devices with large-scale energy storage applications, owing to the advantages of long lifespan, high safety, and decoupled energy and power designs [5]. Until now, various redox batteries have been reported in the literature, including the all-vanadium flow battery, zinc-cerium flow battery, zinc-bromine flow battery, iron-bromine flow battery, and sodium-sulfur battery [6]. Among the flow batteries, the vanadium flow battery (VFB), which is put forward by Skyllas-Kazacos and co-workers [7–9], is one of the most promising choices as the same element (vanadium) is employed in both positive and negative sides, thus avoiding cross-contamination.

In previous decades, many studies have been conducted on vanadium flow batteries to promote their application. On the one hand, the key materials and cell design are well

developed, which contributes to the promotion of strong battery performance [10,11]. On the other hand, operational parameters have also been analyzed to realize an optimal operation strategy, thus further improving the reliability and overall performance of VFBs [12]. Of the critical operational parameters, the flow rate is a factor with a powerful impact on the performance of flow batteries [13]. Accordingly, its effects and regulation strategy have been extensively investigated by researchers. Some researchers optimize the flow rate through experimental methods [14]. However, most efforts in this field are made by simulation to avoid numerous tests. Therefore, optimized flow control strategies are obtained on the basis of VFB models. For instance, a variable flow rate is analyzed via VFB models to realize both high capacity and high efficiency [15,16]. Furthermore, the flow rate is reasonably higher in charging than in discharging [17]. Moreover, the proportional and integral controllers can ensure stable VFB operation at dynamic loads by flow rate regulation [18]. The above studies help the VFBs achieve a favorable flow rate and improve their performance. However, most of the mentioned flow rate optimization is conducted at room temperature. Thus, the obtained operational strategy may lose its applicability if the VFBs are utilized in surroundings of extremely high or low temperature. As a result, it is of great significance for the VFBs to perform a flow rate optimization incorporating temperature impact and subsequently achieving an enhanced overall performance.

In this regard, studies have been conducted to understand the effects of temperature. Skyllas-Kazacos et al. investigated the effects of temperature on ion diffusion [19] and explored electrolyte temperature variations associated with different regional temperature effects using thermal models [20]. Xiong developed an equivalent circuit model considering thermal effects to predict the VFB performance under variable temperature conditions [21]. However, these works do not cover temperature effects on flow rate management. Thus, more complicated models are proposed by researchers to combine the effects of flow rate and temperature. For instance, Tang analyzed the effects of flow rate on the VFB temperature variations using thermal models [22,23]. However, the effects on cell efficiency and capacity were not included. To address such issues, several studies have been conducted on the improvement of VFB performance by optimizing the flow rate and incorporating temperature effects. It was found that the high flow rate benefited from the promotion of heat transfer between electrolyte and cell, which is highly beneficial to the VFBs used in cold climates [24]. Moreover, a relatively high flow rate can also help the VFBs to reduce the temperature increase during charging–discharging [25]. Furthermore, the increased temperature and flow rate can notably enhance the electron transfer coefficient [26]. These works have revealed that the optimal flow rate regulation can be achieved only if the temperature effects are accounted for. However, the two most influential factors, which are cell resistance and electrolyte viscosity, have not been included in the previous studies. On the one hand, the cell resistance has a powerful impact on the cell power at a specific current density which can affect the flow rate strategy. On the other hand, the viscosity can directly influence the pumping energy related to the pressure loss. Thus, it can be a vital complement to the flow rate optimization and has great potential to enhance the performance of VFBs when considering the two issues. Unfortunately, no such reports can be seen in the literature until now.

In this paper, the flow rate optimization is investigated for the first time for vanadium flow batteries using a dynamic model which considers the variation of cell resistance and electrolyte viscosity versus temperature. To start with, a dynamic VFB model is developed based on mass conservation. Next, two applied flow rates are used to validate the proposed dynamic model. Afterwards, the effects of temperature on electrolyte viscosity and internal resistance, and the flow rate optimization incorporating such effects, are thoroughly evaluated. The simulation results demonstrate that the variations of electrolyte viscosity and internal resistance associated with the variations of temperature significantly impact the flow rate strategy. Moreover, the maximum system efficiency at each specific temperature is increased with the increase in temperature, but are obtained at different flow rates.

Three sections are represented in the following paper. A description of the experimental methods can be found in Section 2, including materials, electrolyte preparation, cell test, and dynamic modeling. Subsequently, a discussion of the results of temperature and flow rate optimization is stated in Section 3. In Section 4, the conclusions are described.

2. Experimental

2.1. Materials

The membranes (Nafion 212) used in this work were purchased from DuPont Co., Ltd. (Shanghai, China). Porous electrodes (JinGu-42) were purchased from Liaoning Jingu Carbon Materials Co., Ltd. (Liaoyang, China). Bipolar plates (KVFP1010) were received from Liaoning Kejing New Materials Technology Co., Ltd. (Shenyang, China). Sulfuric acid, stannous chloride, and ferrous chloride of analytical reagent grade were obtained from Sinopharm (Shenyang, China).

2.2. Electrolyte Preparations

Deionized water was used to prepare the electrolytes for the charging–discharging tests. In both half-cells, the electrolyte concentration was 1.7 M $V^{3.5+}$ and 3 M H_2SO_4 .

2.3. Cell Tests

A schematic of a vanadium flow battery is depicted in Figure 1, in which two external tanks are used to carry vanadium ions in their various oxidation states (V^{2+} , V^{3+} , VO^{2+} , and VO_2^+) with one redox pair present in each tank. Throughout the duration, the electrodes and electrolytes that possess VO^{2+} and VO_2^+ are referred to as the positive side. The opposite happens with negative electrolytes and electrodes. The electrolytes are circulated between separated half-cells within the cell and storage tanks. Each half-cell contains a bipolar plate and an electrode; a membrane between two half-cells enables selective ion exchange while limiting electrolyte cross-contamination [27]. The following is an expression for the electrochemical reactions on both the negative and positive sides:

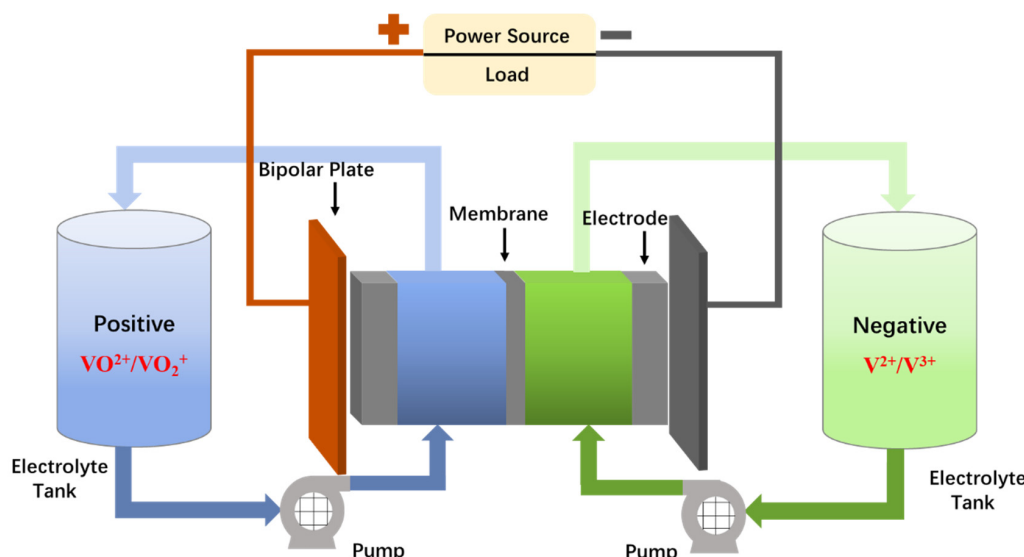
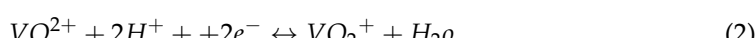


Figure 1. Schematic representations of a vanadium flow battery system.

On the negative side:



On the positive side:



To validate the proposed VFB model, a laboratory flow cell with an area of 28 cm² was prepared and tested. A Neware CT-3008 5 V/12 A cell tester was used to test the cells. The charging–discharging test was fixed to be 100 mA cm⁻² between 1 V and 1.7 V. Each side was filled with 50 mL of electrolytes. Flow rates of 50 mL min⁻¹ and 10 mL min⁻¹ were used, respectively, to validate the model. The detailed specifications are shown in Table 1. Flow cell efficiencies can be determined according to Equations (3)–(5):

$$\text{coulombic efficiency} = \frac{\int I_d dt}{\int I_c dt} \times 100\% \quad (3)$$

$$\text{energy efficiency} = \frac{\int U_d I_d dt}{\int U_c I_c dt} \times 100\% \quad (4)$$

$$\text{voltage efficiency} = \frac{\text{energy efficiency}}{\text{coulombic efficiency}} \times 100\% \quad (5)$$

where:

- *coulombic efficiency* denotes the ratio of the electric charge discharged from a flow cell compared to the electric charge provided during the preceding charge;
- *energy efficiency* is the ratio of the electrical energy provided from the flow cell during discharge to the electrical energy supplied to the flow battery during the preceding charge;
- *voltage efficiency* denotes the ratio of the average discharge voltage to the average charge voltage;
- t_d and t_c denote the process time of discharging and charging, respectively;
- U_d and U_c denote the voltage of discharging and charging, respectively;
- I_d and I_c denote the current of discharging and charging, respectively.

Table 1. Operating parameters and cell geometry.

Parameters	Value
Total concentration of vanadium	1.7 mol L ⁻¹
Flow rate	10 mL min ⁻¹ and 50 mL min ⁻¹
Voltage range	1 V–1.7 V
Electrode dimension	4.2 mm × 4 cm × 7 cm
Electrolyte volume	50 mL
Applied current density	100 mA cm ⁻²

2.4. Dynamic Modeling

2.4.1. Electrochemical Model

The cell voltage of a VFB can be obtained by summing the open-circuit voltage (E_{cell}), the ohmic loss (IR_{cell}), the activation polarization (η_{act}), and the concentration polarization (η_{con}) as expressed in the form of Equation (6):

$$E_{cell} = E_{ocv} + \eta_{act} + \eta_{con} + IR_{cell} \quad (6)$$

where E_{ocv} and η_{con} can be further expressed as Nernst Equation (Equation (7)) and Concentration Polarization Equation (Equation (8)):

$$E_{ocv} = E^{0'} + \frac{RT}{zF} \ln \frac{c_{V(II)} c_{V(V)}}{c_{V(III)} c_{V(IV)}} \quad (7)$$

$$\eta_{con} = \eta_{con}^+ + \eta_{con}^- = \frac{RT}{zF} \ln \left(1 - \frac{i}{zFk_m c_r^+} \right) + \frac{RT}{zF} \ln \left(1 - \frac{i}{zFk_m c_r^-} \right) \quad (8)$$

where:

- $E^{0'}$ is the cell formal potential;
- F and R refer to the Faraday constant and the molar gas constant, respectively;
- T is the temperature;
- z is the unit activity coefficient;
- $c_{V(II)}$, $c_{V(III)}$, $c_{V(IV)}$, and $c_{V(V)}$ are the concentrations of V^{2+} , V^{3+} , VO^{2+} , and VO_2^+ in the cell, respectively;
- c_r^+ and c_r^- are the reactant concentrations in positive and negative half-cells, respectively;
- i is the current density;
- k_m is the local mass transfer coefficient, and is described in the form of Equation (9), where A_1 is the cross-sectional area for electrodes and Q is the flow rate.

$$k_m = 1.6 \times 10^{-4} \frac{Q}{A_1} \quad (9)$$

The η_{act} can be commonly calculated according to the Butler–Volmer equation as shown in Equation (10). Porous electrodes are employed in flow batteries because their surface area can be hundreds of times more than their geometric are, thus giving rise to low actual current density. The η_{act} can be commonly small in flow cells [27]. Additionally, according to Equation (10), one of the key factors that determines the activation overpotential is the current. As a result, Equation (11) is used to construct a novel description of overall ohmic drop that incorporates ohmic loss and cell activation overpotential:

$$i = i_0 \left\{ \exp \left[\frac{\alpha_a n F \eta_{act}}{RT} \right] - \exp \left[\frac{\alpha_c n F \eta_{act}}{RT} \right] \right\} \quad (10)$$

$$IR'_{cell} = IR_{cell} + \eta_{act} \quad (11)$$

where R'_{cell} denotes the defined overall ohmic, i_0 is the exchange current density, and α_c and α_a are the charge transfer coefficients of positive and negative electrodes, respectively.

As a result, the cell voltage can be calculated using Equations (12) and (13) as follows.
For charging:

$$E_{cell} = E^{0'} + \frac{RT}{zF} \ln \frac{c_{V(II)} c_{V(V)}}{c_{V(III)} c_{V(IV)}} + \left| \frac{RT}{zF} \ln \left(1 - \frac{i}{1.6 \times 10^{-4} \frac{Q}{A_1} z F c_r^+} \right) \right| + \left| \frac{RT}{zF} \ln \left(1 - \frac{i}{1.6 \times 10^{-4} \frac{Q}{A_1} z F c_r^-} \right) \right| + IR'_{cell} \quad (12)$$

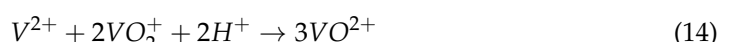
For discharging:

$$E_{cell} = E^{0'} + \frac{RT}{zF} \ln \frac{c_{V(II)} c_{V(V)}}{c_{V(III)} c_{V(IV)}} - \left| \frac{RT}{zF} \ln \left(1 - \frac{i}{1.6 \times 10^{-4} \frac{Q}{A_1} z F c_r^+} \right) \right| - \left| \frac{RT}{zF} \ln \left(1 - \frac{i}{1.6 \times 10^{-4} \frac{Q}{A_1} z F c_r^-} \right) \right| - IR'_{cell} \quad (13)$$

2.4.2. Mass Balance

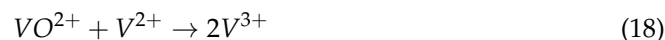
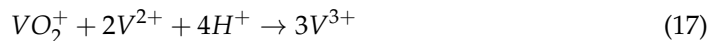
To facilitate the mass balance, the effects of ion diffusion across membranes are analyzed first. Since there is always a vanadium ion concentration imbalance between the negative and positive electrolytes, the crossing of vanadium ions through the membrane cannot be avoided in practice. As a result, each electrolyte undergoes the self-discharge processes that leads to a reduction in capacity. Concerning ion diffusion, all of the vanadium ions in four distinct oxidation states move across the membrane and interact with one another, resulting in the reactions illustrated below [28].

The following self-discharge processes will occur in the positive side owing to the diffusion of V^{2+} and V^{3+} ions from the negative side:





While VO_2^+ and VO^{2+} ions from the positive side will behave thusly in the negative side:



Fick's first law, which is demonstrated below, enables the above effects by stating that the flux of diffusion is from a region of high concentration to a region of low concentration, with a magnitude proportional to the concentration gradient:

$$J = -k \frac{dc}{dx} \quad (20)$$

where J is the diffusion flux ($\text{mol L}^{-1} \text{s}^{-2}$), k is the diffusion coefficient (ms^{-1}), dc is the concentration difference across the membrane (mol L^{-1}), and dx is the diffusion layer thickness which is assumed to be equal to the thickness of the membrane (m). As a result, the dynamic model could be constructed using the research presented above and the accompanying assumptions:

- (1) The electrolyte concentrations are uniform in the cell/stack and tank.
- (2) Gassing side reactions can be minimized.
- (3) Throughout the operation, the reservoirs, cells, and stacks are maintained at a constant 25 °C.
- (4) The proton concentration in each half-cell electrolyte remains constant during charge-discharge cycling.
- (5) The variations of electrolyte volume in the cell/stack and reservoirs are negligible.

Taking VO_2^+ as an example, if the electrolyte flow rate is ignored, its concentration can be estimated by computing its time derivatives as expressed in Equation (21).

$$\frac{dc_{V(V)}(t)}{dt} = \pm \frac{I}{zF} - \frac{A_2}{\theta} (k_5 c_{V(V)} + 2k_2 c_{V(II)} + k_3 c_{V(III)}) \quad (21)$$

Further, if the flow rate is taken into account, the concentrations of VO_2^+ in the cell and tank can be calculated according to Equation (22):

- for VO_2^+ ions:

$$\begin{cases} V \frac{dc_{V(V)}(t)}{dt} = Q(c'_{V(V)} - c_{V(V)}) \pm \frac{I}{zF} - \frac{A_2}{\theta} (k_5 c_{V(V)} + 2k_2 c_{V(II)} + k_3 c_{V(III)}) \\ V' \frac{dc_{V(V)}(t)}{dt} = Q(c_{V(V)} - c'_{V(V)}) \end{cases} \quad (22)$$

Similarly, for the other three types of vanadium ions, their concentrations can be obtained using Equations (23)–(25):

- for VO^{2+} ions:

$$\begin{cases} V \frac{dc_{V(V)}(t)}{dt} = Q(c'_{V(V)} - c_{V(V)}) \pm \frac{I}{zF} - \frac{A_2}{\theta} (k_5 c_{V(V)} + 2k_2 c_{V(II)} + k_3 c_{V(III)}) \\ V' \frac{dc_{V(V)}(t)}{dt} = Q(c_{V(V)} - c'_{V(V)}) \end{cases} \quad (23)$$

- for V^{3+} ions:

$$\begin{cases} V \frac{dc_{V(III)}(t)}{dt} = Q(c'_{V(III)} - c_{V(III)}) \mp \frac{I}{zF} - \frac{A_2}{\theta} (k_3 c_{V(III)} - 2k_4 c_{V(IV)} - 3k_5 c_{V(V)}) \\ V' \frac{dc'_{V(III)}(t)}{dt} = Q(c_{V(III)} - c'_{V(III)}) \end{cases} \quad (24)$$

- for V^{2+} ions:

$$\begin{cases} V \frac{dc_{V(II)}(t)}{dt} = Q(c'_{V(II)} - c_{V(II)}) \pm \frac{I}{zF} - \frac{A_2}{\theta} (k_2 c_{V(II)} + k_4 c_{V(IV)} + 2k_5 c_{V(V)}) \\ V' \frac{dc'_{V(II)}(t)}{dt} = Q(c_{V(II)} - c'_{V(II)}) \end{cases} \quad (25)$$

where:

- $c'_{V(V)}$, $c'_{V(IV)}$, $c'_{V(III)}$, and $c'_{V(II)}$ are the concentration of VO_2^+ , VO^{2+} , V^{3+} , and V^{2+} in reservoir, respectively;
- V is the electrolyte volume in the cell;
- V' is the electrolyte volume in the tank;
- A_2 is the cross-sectional area of the membrane;
- θ is the thickness of the membrane;
- k_2 , k_3 , k_4 , and k_5 are the diffusion coefficients of V^{2+} , V^{3+} , VO^{2+} , and VO_2^+ , respectively;
- “+” and “-” are the processes of charging and discharging, respectively.

The flow rate Q can be obtained using Equation (26), where f denotes the flow factor and c_r , in the case of constant flow rate control, denotes the reactant concentration at the end of charge/discharge as defined by Equation (27).

$$Q = f \frac{|I|}{Fc_r} \quad (26)$$

$$c_r = c_r(t_{\text{end}}) \quad (27)$$

The flow factor is a ratio between the flux of charges provided by the electrolyte flow for the reactions and the electric current generated in the cell [29]. In particular, it depends linearly on I and inversely on Q . Thus, for constant current operational conditions, the regulation of flow rate is equivalent to the regulation of flow factor. $f = 1$ would be the ideal condition with regard to minimizing the pumping power. However, it is usually kept at values larger than 1, to ensure proper electrolyte reactions [12]. Hence, the flow factor should be optimized in practice to enhance the overall performances of VFBs.

2.5. Pressure Loss, Pump Loss, and System Efficiency

2.5.1. Pressure Loss in Flow Cell

By assuming that the pressure loss of a flow battery is caused by the pipe and carbon felt, the pressure loss can be expressed as Equation (28):

$$\Delta P_{\text{total}} = \Delta P_{\text{felt}} + \Delta P_{\text{pipe}} \quad (28)$$

where:

1. P_{total} is the overall pressure loss of the flow battery.
2. ΔP_{pipe} is the pressure loss through the pipe.
3. The pressure loss through a porous electrode, denoted by ΔP_{felt} , may be calculated using Darcy's equation, as shown in Equations (29) and (30):

$$\Delta P_{\text{felt}} = \frac{\mu l Q}{\kappa A} \quad (29)$$

$$\kappa = \frac{d_f^2}{16K} \frac{\varepsilon^3}{(1-\varepsilon)^2} \quad (30)$$

where:

- l denotes electrode length;
- A denotes electrode cross-sectional area;
- μ denotes electrolyte viscosity;
- d_f denotes fiber diameter;
- κ denotes electrode permeability;
- ε denotes electrode porosity.

The Darcy–Weisbach equation can also be used to measure the pressure loss via a pipe in the form of Equation (31):

$$\Delta P_{\text{pipe}} = f_D \frac{L}{D} \frac{\rho v^2}{2} \quad (31)$$

where:

- f_D is the Darcy friction factor;
- D is the pipe diameter;
- v is the velocity of the flow;
- L is the pipe length.

f_D can be stated as an Equation (32).

$$f_D = \frac{64}{Re} \quad (32)$$

Re is the Reynolds number expressed in Equation (33), where A_p is the cross-sectional area.

$$Re = \frac{\rho D Q}{\mu A_p} \quad (33)$$

Equation (34) can be used as a replacement for Equation (23), since it is preferred to represent pressure loss in a pipe as the volumetric flow rate.

$$v^2 = \frac{Q^2}{A_p^2} \quad (34)$$

2.5.2. Pump Loss and System Efficiency

Equation (35) may be used to describe the pump power, where the operating circumstances and the pump configuration determine the pump efficiency α (assumed to be 80 percent in this paper).

$$P_{\text{pump}} = \frac{\Delta P_{\text{total}} Q}{\alpha} \quad (35)$$

As a result, given operating circumstances involving constant current, the total energy needed for charging or deliverable for discharging is represented as Equation (36).

$$W = I \cdot \int_0^t E_{\text{cell}}(t) dt \pm \int_0^t P_{\text{pump}}(t) dt \quad (36)$$

Accordingly, Equation (37) may be used to calculate the flow battery system efficiency.

$$\text{System efficiency} = \frac{W_{\text{discharge}}}{W_{\text{charge}}} \quad (37)$$

3. Results and Discussion

3.1. Model Validation

To start with, Figure 2a,b illustrates the actual and simulated cell voltages for a 28 cm^2 flow cell used in the model validation at flow rates of 10 mL min^{-1} and 50 mL min^{-1} , respectively. As can be observed, the experimental voltages and the simulated voltages at the two flow rates are well-matched. Thus, it is indicated that the proposed model can capture the electrochemical properties of VFBs. Figure 2a,b further illustrates how varied operational circumstances can lead to significant variations in cell behaviors for VFBs. Therefore, conducting a comprehensive study to optimize the operating strategy is crucial to obtaining improved overall performance for vanadium flow batteries.

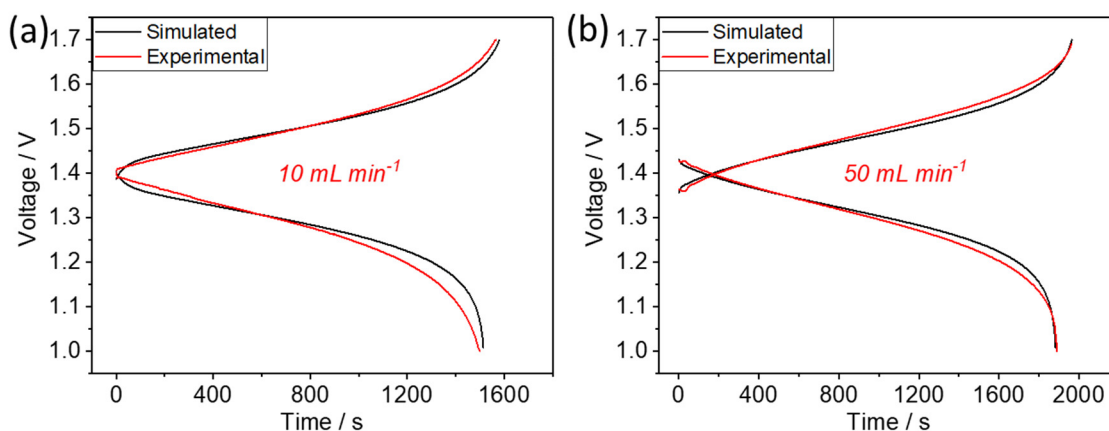


Figure 2. Simulated and experimental voltage at (a) 10 mL min^{-1} and (b) 50 mL min^{-1} .

Following the validation of the modeling, a 30 kW VFB stack with a 4500 cm^2 effective area is involved in the simulation. In Sections 3.2 and 3.3, which follow, the effects of temperature and flow rate optimization incorporating temperature effects are investigated in depth. Table 2 provides details on the particular stack geometry and model parameters.

Table 2. Simulation parameters and stack specifications.

Parameters	Value
Electrolyte volume	400 L
Vanadium concentration	1.7 mol L^{-1}
Number of cells in the stack	60
Cut-off for charging/discharging	SOC = 90%/10%
Diffusion coefficient of V^{2+}	3.125×10^{-12}
Diffusion coefficient of V^{3+}	5.93×10^{-12}
Diffusion coefficient of VO^{2+}	5.0×10^{-12}
Diffusion coefficient of VO_2^+	1.17×10^{-12}
Electrode porosity	93%
Electrode size	$900\text{ mm} \times 500\text{ mm} \times 4.2\text{ mm}$
Flow rate	$5\text{ m}^3 \text{ h}^{-1}$
Temperature	298.15 K
Cell formal potential	1.4 V

3.2. Effects of Temperature

3.2.1. Effects of Temperature on Viscosity

To facilitate the simulation, the electrolyte viscosity is assumed to be constant with the variation of SOC and equal to that at the SOC of 50%. With the above assumption, the simulation is conducted to understand the impacts of temperature on electrolyte viscosity and the battery performance of VFBs. According to previous studies [30], the electrolyte viscosities, which can be significantly impacted by temperature, are illustrated in Figure 3a.

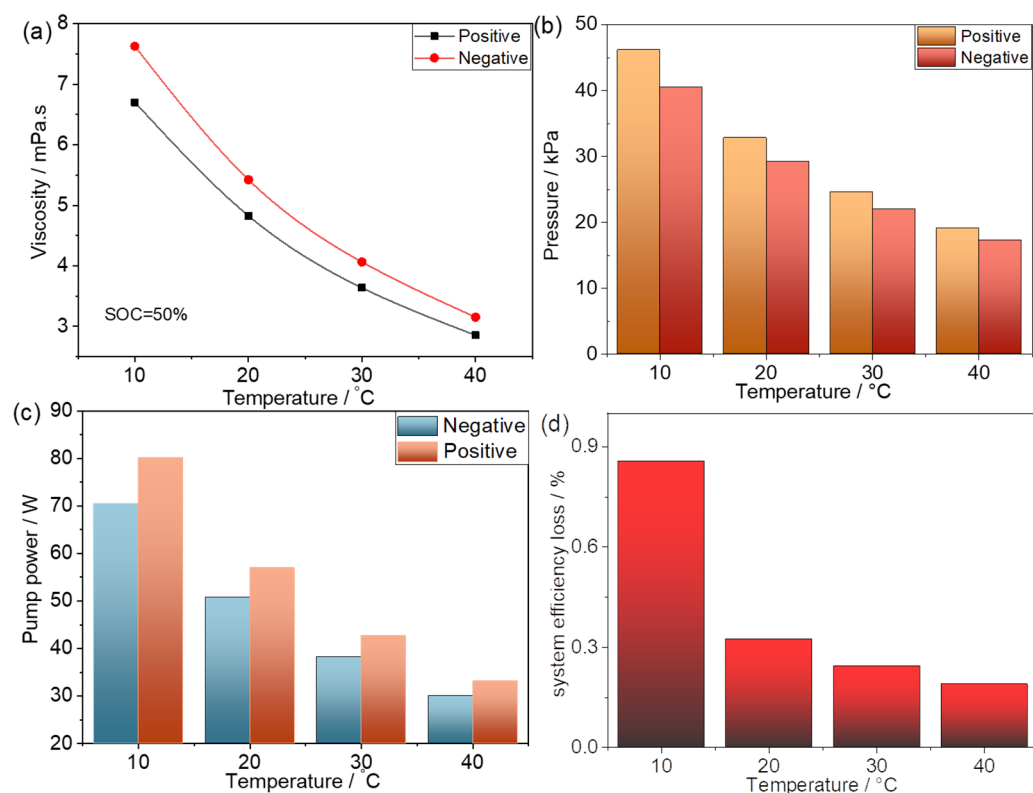


Figure 3. (a) Viscosity at different temperatures and its effects on (b) stack pressure, (c) pump power, and (d) system efficiency loss.

As can be seen, both the viscosities for positive electrolytes and negative electrolytes are notably decreased with the increase in temperature. For instance, the viscosity at 40 °C is less than half that at 10 °C for both sides. Such changes in viscosity can significantly affect the pressure drop. Thus, the pressure drop is calculated according to Darcy's law, and the pressure drop versus temperature is demonstrated in Figure 3b. Not surprisingly, the pressure drop noticeably decreases as the temperature increases. Moreover, the pressure drop can further affect the loss of pump power according to Equation (27). As can be observed in Figure 3c, the pump loss in the positive and negative sides dramatically declines with the increase in temperature. In particular, as the temperature increases from 10 °C to 40 °C, the pump loss decreases to approximately 58% from 80 kPa to 33 kPa for the negative side, and from 70 kPa to 30 kPa for the positive side. Thus, the system efficiency can be different at different temperatures if incorporating pump loss. The system efficiency loss caused by the pump energy loss at different temperatures is demonstrated in Figure 3d. As expected, a low temperature with high electrolyte viscosity results in high system efficiency loss. Especially at a temperature of 10 °C, the system efficiency loss reaches up to over twice that at 20 °C. While at a temperature over 20 °C, the system efficiency losses are relatively low and of slight variation. Hence, it is preferable for the VFBs to be applied at a temperature above 20 °C. Furthermore, as the electrolyte viscosity associated with temperature can powerfully affect the system efficiency, for actual VFB systems to achieve improved overall performance, the flow rate should be regulated effectively while accounting for viscosity change.

3.2.2. Effects of Temperature on Internal Resistance

Apart from the above-discussed electrolyte viscosity, the internal resistance can also be influenced by temperature and be capable of affecting the overall performance of VFBs. The stack resistance used in this work was obtained according to our previous study [31], in which the area-specific resistance of VFBs at 10 °C, 20 °C, 30 °C, and 40 °C was 0.89 Ω·cm², 0.80 Ω·cm², 0.73 Ω·cm², and 0.66 Ω·cm², respectively. Thus, the stack voltage can be

different at different temperatures with the variable resistance. Figure 4a shows the stack voltages at different temperatures, where the voltage decreases in charging and increases in discharging as the temperature increases. As a result, the stack efficiency can also be different and is analyzed as shown in Figure 4b. As observed, the energy efficiency increases with the increase in temperature due to the decrease in cell resistance at high temperatures. More specifically, as the temperature increases from 10 °C to 40 °C, the energy efficiency of the stack increases up to 2.6%. In addition to the energy efficiency, the lowered resistance can also help the VFB to enhance its discharging power. Figure 4c illustrates the average stack discharge power for each specific temperature, which is enhanced from 34.5 kW to 35.1 kW when the temperature rises from 10 °C to 40 °C. Furthermore, the high temperature can be beneficial to the stack pressure owing to the lowered electrolyte viscosity, as discussed in Section 3.2.1, which has great potential for the VFBs to realize an outstanding system efficiency. The system efficiency is investigated and shown in Figure 4d, where it notably increases as the temperature increases. On the one hand, a relatively high temperature is preferable for the VFBs to achieve a higher system efficiency, benefiting from the lowered electrolyte viscosity and stack resistance. On the other hand, due to the variation of electrolyte viscosity and stack resistance and their powerful impacts on stack performance, the flow rate regulation is able to be optimized with the variation of temperature, such that a more advanced flow rate strategy and an improved overall performance of VFB can be both obtained.

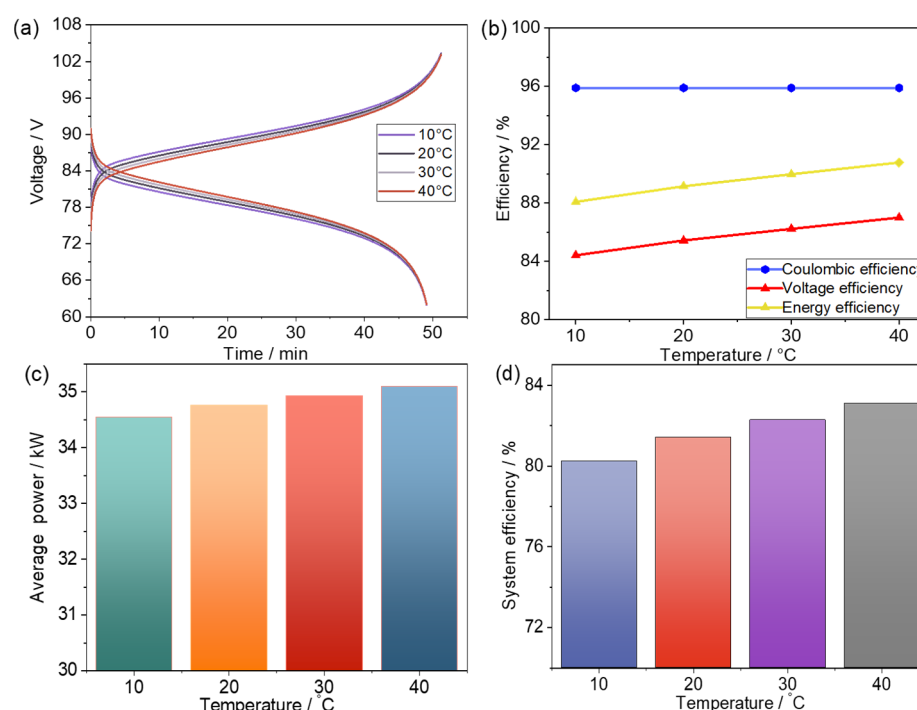


Figure 4. Effects of internal resistance on (a) voltage, (b) efficiency, (c) average power, and (d) system efficiency.

3.3. Optimization of Flow Rate

3.3.1. Charging–Discharging Behavior

One of the crucial elements that affects VFBs' operation is the electrolyte flow rate. Commonly, a proper flow rate is required to avoid adverse effects and reduce concentration over potential losses. On the other hand, additional pumping energy use may result from an excessive flow rate. Hence, in actual application, the flow rate should be carefully controlled. To determine the appropriate flow rate of VFBs throughout a broad temperature range and therefore improve their overall performances, the influences of flow rate are thus examined in this section. Figure 5a–d show the stack voltages with the various flow

factors at temperatures from 10 °C to 40 °C, respectively. As observed at each specific temperature, the stack voltages are higher at a larger flow rate in the discharging process and lower at a smaller flow rate in the charging process, particularly at charge or discharge termination. This can be attributed to the high concentration polarization at a low flow rate [32]. Despite such similar tendencies, there is still a difference in the voltage curves obtained at different temperatures. For instance, the stack voltage at the beginning of the discharge process increases from 88.5 V to 91 V as the temperature rises from 10 °C to 40 °C at the same flow factor of one. As a result, the stack performance can be different at each specific temperature and flow rate. Thus, it is of significance to perform a flow rate investigation and obtain the optimal flow rate for different temperatures.

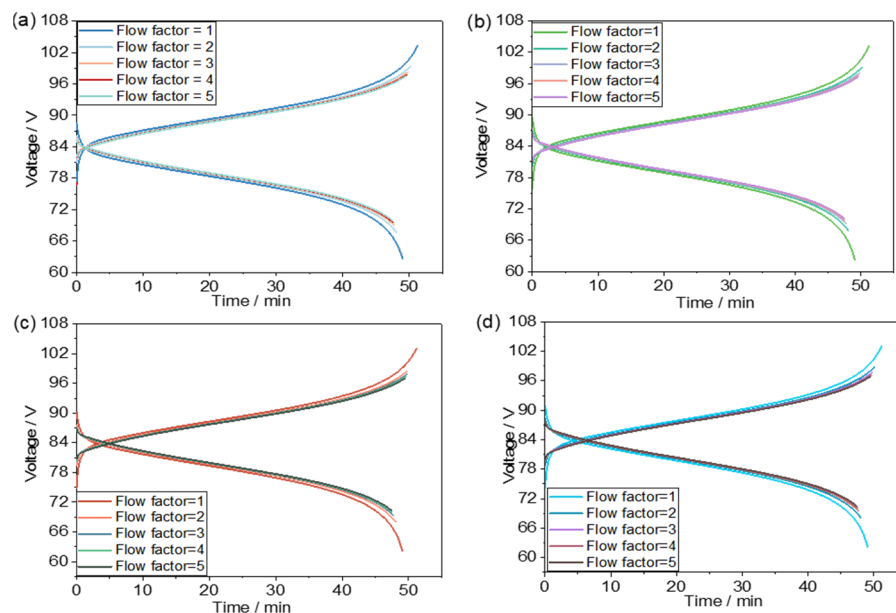


Figure 5. Effect of flow rate on stack voltages at (a) 10 °C, (b) 20 °C, (c) 30 °C, and (d) 40 °C.

3.3.2. Optimal System Efficiency and Flow Rate

To analyze the effects of flow rate at different temperatures in detail, the efficiencies of the VFB stack are investigated. The coulombic efficiencies of the stack are shown in Figure 6a, where there is little difference among the obtained coulombic efficiencies. Moreover, the voltage efficiencies of the stack are also calculated and depicted in Figure 6b. As anticipated, the voltage efficiency improves with an increase in temperature due to the clearly reduced internal resistance and with a growing flow rate because of the decreased concentration polarization. As a result, the energy efficiency, being the product of voltage efficiency and coulombic efficiency, represents a similar variation with the voltage efficiency, as illustrated in Figure 6c. However, the high flow rate can lead to additional stack pressure and pump loss. The stack pressures at each flow factor and temperature are illustrated in Figure 6d. As observed, at low temperatures and high flow rates, the stack pressures are significantly higher than those at high temperatures and low flow rates. For instance, a stack pressure of 10 °C and a flow factor of 5 is about 12 times higher than that of 40 °C and a flow factor of 1. As a consequence, the pump loss can be greatly different as well, as shown in Figure 6e. As observed, the pump power significantly increases with the increase inflow rate and a decrease in temperature. Thus, the system efficiency incorporating the pump loss can be highly influenced. As depicted in Figure 6f, the system efficiency is higher overall at higher temperatures. However, the highest system efficiency for each specific temperature can be obtained at different flow factors. For a clearer representation, the maximum system efficiency and correspondingly optimal flow rate are shown in Figure 7a,b. As observed in Figure 7a, the maximum system efficiency at each specific temperature increases from 80.3% to 83.8% as the temperature increases from 10 °C to 40 °C. It is not a surprise that

the maximum system efficiency increases with the temperature. This result shows that the maximum system efficiency at each specific temperature is obtained at different flow factors. The optimal flow factor for different temperatures is depicted in Figure 7b. As observed, the optimal flow factor for 10 °C is one, while for the other three temperatures it is two. Thus, the flow rate strategy of VFBs needs to be different if operated at different temperatures. Furthermore, a comparatively high flow rate is preferred for use at high temperatures, whereas a relatively low flow rate is acceptable for use at low temperatures. It is of significance for practical VFBs to realize an optimized flow rate and subsequently enhance their comprehensive performance in complex temperature conditions.

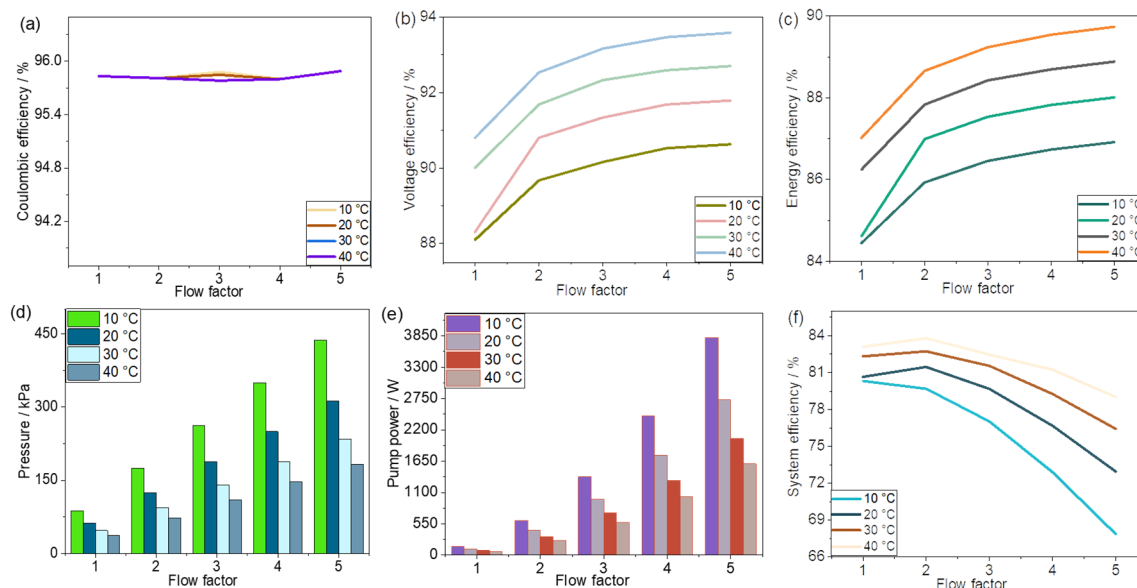


Figure 6. Effect of flow rate on (a) coulombic efficiency, (b) voltage efficiency, (c) energy efficiency, (d) stack pressure, (e) pump power, and (f) system efficiency at different temperatures.

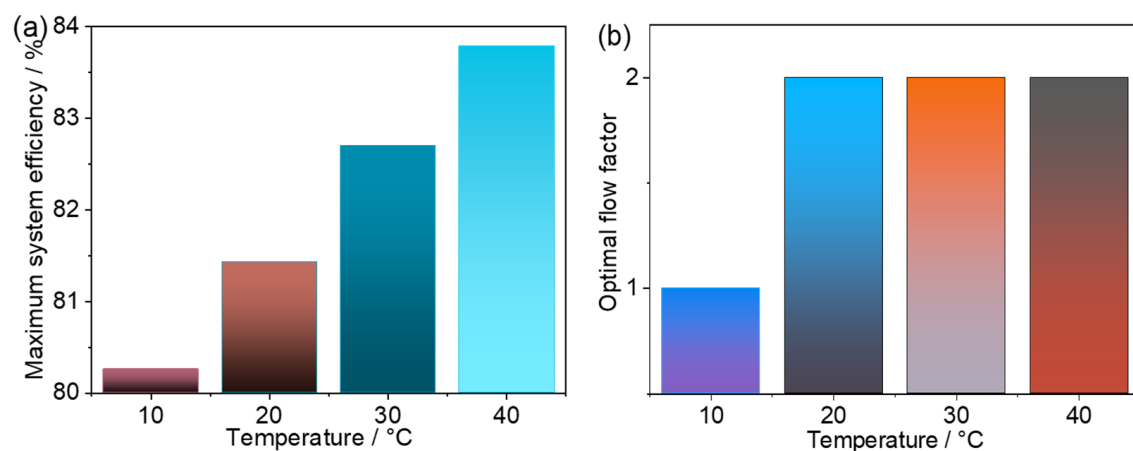


Figure 7. (a) Maximum system efficiency and (b) optimal flow factor incorporating temperature effect.

4. Conclusions

This research revealed a dynamic model focused on mass conservation to improve flow rate while accounting for the impact of temperature, thereby improving VFB performances. To facilitate the simulation, the system used in this work was a 30 kW VFB with 60 single cells, and the findings suggest that the electrolyte viscosity and cell resistance both decrease with the increase in temperature, thus notably affecting flow rate regulation. In addition, the

maximum system efficiency increased as the temperature increased. Moreover, the optimal flow factor at 10 °C and over 20 °C was one and two for the VFBs, respectively. Such an in-depth investigation is of solid significance for vanadium flow batteries to optimize their flow rate. In addition, a cost-effective method is successfully provided by the proposed dynamic model, thereby minimizing repeated field tests, extended testing periods, and the consumption of considerable electrical energy.

Author Contributions: Conceptualization, H.C. and F.C.; methodology, L.H.; software, L.H.; validation, X.C. and Q.H.; formal analysis, X.C. and Q.H.; investigation X.C. and Q.H.; resources, F.C.; writing—original draft preparation, L.H. and H.C.; writing—review and editing, F.C.; supervision, Q.Z.; funding acquisition, F.C. and Q.Z. All authors have read and agreed to the published version of the manuscript.

Funding: This research was funded by the National Natural Science Foundation of China [No. 12274361 and No. 22005263], the Natural Science Foundation of Jiangsu Province (BK20211361), College Natural Science Research Project of Jiangsu Province (20KJA430004).

Institutional Review Board Statement: Not applicable.

Informed Consent Statement: Not applicable.

Data Availability Statement: Data sharing not applicable.

Conflicts of Interest: The authors declare no conflict of interest.

References

1. Zhao, Z.; Zhang, C.; Li, X. Opportunities and challenges of organic flow battery for electrochemical energy storage technology. *J. Energy Chem.* **2022**, *67*, 621–639. [[CrossRef](#)]
2. Parasuraman, A.; Lim, T.M.; Menictas, C.; Skyllas-Kazacos, M. Review of material research and development for vanadium redox flow battery applications. *Electrochim. Acta* **2013**, *101*, 27–40. [[CrossRef](#)]
3. Khaki, B.; Das, P. Multi-objective optimal charging current and flow management of Vanadium Redox Flow Batteries for fast charging and energy-efficient operation. *J. Power Sources* **2021**, *506*, 230199. [[CrossRef](#)]
4. Trovò, A. Battery management system for industrial-scale vanadium redox flow batteries: Features and operation. *J. Power Sources* **2020**, *465*, 228229. [[CrossRef](#)]
5. Emmett, R.K.; Roberts, M.E. Recent developments in alternative aqueous redox flow batteries for grid-scale energy storage. *J. Power Sources* **2021**, *506*, 230087. [[CrossRef](#)]
6. Li, Z.; Jiang, T.; Ali, M.; Wu, C.; Chen, W. Recent Progress in Organic Species for Redox Flow Batteries. *Energy Storage Mater.* **2022**, *50*, 105–138. [[CrossRef](#)]
7. Khaki, B.; Das, P. Voltage loss and capacity fade reduction in vanadium redox battery by electrolyte flow control. *Electrochim. Acta* **2022**, *405*, 139842. [[CrossRef](#)]
8. Chen, H.; Su, M.; Liu, Y.; Chen, Z.; Chen, F. In-Depth Analysis of Transport Delay on Cell Performance and Modeling Precision for All-Vanadium Flow Battery. *J. Electrochem. Soc.* **2021**, *168*, 060546. [[CrossRef](#)]
9. Huang, Z.; Mu, A.; Wu, L.; Wang, H. Vanadium redox flow batteries: Flow field design and flow rate optimization. *J. Energy Storage* **2022**, *45*, 103526. [[CrossRef](#)]
10. Javed, M.S.; Zhong, D.; Ma, T.; Song, A.; Ahmed, S. Hybrid pumped hydro and battery storage for renewable energy based power supply system. *Appl. Energy* **2020**, *257*, 114026. [[CrossRef](#)]
11. Chen, H.; Li, X.; Gao, H.; Liu, J.; Yan, C.; Tang, A. Numerical modelling and in-depth analysis of multi-stack vanadium flow battery module incorporating transport delay. *Appl. Energy* **2019**, *247*, 13–23. [[CrossRef](#)]
12. Tang, A.; Bao, J.; Skyllas-Kazacos, M. Studies on pressure losses and flow rate optimization in vanadium redox flow battery. *J. Power Sources* **2014**, *248*, 154–162. [[CrossRef](#)]
13. Trovo, A.; Guarnieri, M. Battery management system with testing protocols for kW-class vanadium redox flow batteries. In Proceedings of the 2020 2nd IEEE International Conference on Industrial Electronics for Sustainable Energy Systems (IESES), Cagliari, Italy, 1–3 September 2020; pp. 33–38. [[CrossRef](#)]
14. Ma, X.; Zhang, H.; Sun, C.; Zou, Y.; Zhang, T. An optimal strategy of electrolyte flow rate for vanadium redox flow battery. *J. Power Sources* **2012**, *203*, 153–158. [[CrossRef](#)]
15. Karrech, A.; Regenauer-Lieb, K.; Abbassi, F. Vanadium flow batteries at variable flow rates. *J. Energy Storage* **2022**, *45*, 103623. [[CrossRef](#)]
16. Wang, W.; Tian, L. Control strategy optimization of electrolyte flow rate for all vanadium redox flow battery with consideration of pump. *Renew. Energy* **2018**, *133*, 1445–1454.
17. König, S.; Suriyah, M.R.; Leibfried, T. Innovative model-based flow rate optimization for vanadium redox flow batteries. *J. Power Sources* **2016**, *333*, 134–144. [[CrossRef](#)]

18. Pugach, M.; Parsegov, S.; Gryazina, E.; Bischi, A. Output feedback control of electrolyte flow rate for Vanadium Redox Flow Batteries. *J. Power Sources* **2020**, *455*, 227916. [[CrossRef](#)]
19. Badrinarayanan, R.; Zhao, J.; Tseng, K.; Skyllas-Kazacos, M. Extended dynamic model for ion diffusion in all-vanadium redox flow battery including the effects of temperature and bulk electrolyte transfer. *J. Power Sources* **2014**, *270*, 576–586. [[CrossRef](#)]
20. Tang, A.; Skyllas-Kazacos, M. Simulation Analysis of Regional Temperature Effects and Battery Management Schedules for a Residential-Scale Vanadium Redox Flow Battery System. *Chempluschem* **2015**, *80*, 368–375. [[CrossRef](#)]
21. Xiong, B.; Yang, Y.; Tang, J.; Li, Y.; Wei, Z.; Su, Y.; Zhang, Q. An Enhanced Equivalent Circuit Model of Vanadium Redox Flow Battery Energy Storage Systems Considering Thermal Effects. *IEEE Access* **2019**, *7*, 62297–162308. [[CrossRef](#)]
22. Tang, A.; Ting, S.; Tao, J.; Skyllas-Kazacos, M. Thermal modelling and simulation of the all-vanadium redox flow battery. *J. Power Sources* **2012**, *203*, 165–176. [[CrossRef](#)]
23. Tang, A.; Tao, J.; Skyllas-Kazacos, M. Thermal modelling of battery configuration and self-discharge reactions in vanadium redox flow battery. *J. Power Sources* **2012**, *216*, 489–501. [[CrossRef](#)]
24. Rho, K.H.; Yoon, S.J.; Ryu, J.; Cho, S.M.; Kim, M.S.; Kim, D.K. Study on thermal behavior of vanadium redox flow battery at low temperature to prevent precipitation. *J. Energy Storage* **2022**, *49*, 104110. [[CrossRef](#)]
25. Wang, T.; Fu, J.; Zheng, M.; Yu, Z. Dynamic control strategy for the electrolyte flow rate of vanadium redox flow batteries. *Appl. Energy* **2018**, *227*, 613–623. [[CrossRef](#)]
26. Kim, J.; Park, H. Electrokinetic parameters of a vanadium redox flow battery with varying temperature and electrolyte flow rate. *Renew. Energy* **2019**, *138*, 284–291. [[CrossRef](#)]
27. Lourenssen, K.; Williams, J.; Ahmadpour, F.; Clemmer, R.; Tasnim, S. Vanadium redox flow batteries: A comprehensive review. *J. Energy Storage* **2019**, *25*, 100844. [[CrossRef](#)]
28. Tang, A.; Bao, J.; Skyllas-Kazacos, M. Dynamic modelling of the effects of ion diffusion and side reactions on the capacity loss for vanadium redox flow battery. *J. Power Sources* **2011**, *196*, 10737–10747. [[CrossRef](#)]
29. Li, X.; Xiong, J.; Tang, A.; Qin, Y.; Liu, J.; Yan, C. Investigation of the use of electrolyte viscosity for online state-of-charge monitoring design in vanadium redox flow battery. *Appl. Energy* **2018**, *211*, 1050–1059. [[CrossRef](#)]
30. Guarneri, M.; Trovò, A.; Picano, F. Enhancing the Efficiency of KW-Class Vanadium Redox Flow Batteries by Flow Factor Modulation: An Experimental Method. *Appl. Energy* **2020**, *262*, 114532. [[CrossRef](#)]
31. Chen, H.; Han, L.; Zhang, Y.; Zhang, S.; Chen, F.; Ma, X.; Zhang, Q. Modeling and Optimization of Vanadium Flow Batteries Incorporating Variable Permeability and Resistance. *J. Electrochem. Soc.* **2022**, *169*, 110518. [[CrossRef](#)]
32. Chen, H.; Cheng, M.; Liu, L.; Wang, Y.; Chen, F.; Ma, X.; Zhang, Q. Mathematical modeling and in-depth analysis of 10 kW-class iron-vanadium flow batteries. *J. Power Sources* **2023**, *563*, 232813. [[CrossRef](#)]

Disclaimer/Publisher’s Note: The statements, opinions and data contained in all publications are solely those of the individual author(s) and contributor(s) and not of MDPI and/or the editor(s). MDPI and/or the editor(s) disclaim responsibility for any injury to people or property resulting from any ideas, methods, instructions or products referred to in the content.